

Hybrid k -squared Source Model for Strong Ground Motion Simulations: Introduction

František Gallovič^{1*} and Johana Brokešová¹

¹*Department of Geophysics, Faculty of Mathematics and Physics, Charles University, V Holešovičkách 2, Prague 8, 180 00, Czech Republic*

** Author for correspondence:*

František Gallovič
Department of Geophysics
Faculty of Mathematics and Physics
Charles University
V Holešovičkách 2
Prague 8, 180 00
Czech Republic
e-mail: gallovic@karel.troja.mff.cuni.cz
tel.: +420221912535
fax.: +420221912555

Physics of the Earth and Planetary Interiors (in press).

Abstract

Common kinematic strong motion modeling techniques can be divided into integral and composite according to the source representation. In the integral approach, we usually consider the rupture propagating in the form of a slip pulse, creating the k -squared final slip distribution. Such a model is acceptable on large scales where the faulting process is assumed to be deterministic, which is also supported by low-frequency slip inversions. Nevertheless, on small scales the real rupture is rather disorganized (chaotic) and requires a stochastic description. This is involved in the composite approach, in which the source acts as a discrete sequence of individually rupturing subevents. However, this model usually leads to incorrect spectral amplitudes in the low-frequency band (as compared to the integral model). The purpose of this study is to propose a hybrid kinematic k -squared source model based on a set of subsources, scaled to provide the k -squared slip distribution. The modeling combines 1) the integral approach at low frequencies, based on the representation theorem and the k -squared slip distribution (obtained by composing subsources slip contributions), and 2) the composite approach at high frequencies, based on the summation of ground motion contributions from the subsources, treated as individual point sources. The same set of subsources is used in both the approaches, i.e. for both the frequency ranges. The hybrid method is numerically efficient, while minimizing the above-mentioned problems of both the techniques. The source model is applied to two events: 1999 Athens ($M_w=5.9$) and 1997 Kagoshima ($M_w=6.1$) earthquake examples. In the first example, the simulated PGAs are examined with respect to the attenuation relation for Greece. In the second example, synthetic velocigrams are compared with observed data showing that, despite the neglected site-effects, the complexities of measured waveforms are relatively well reproduced.

Keywords

Strong ground motions; kinematic source modeling; composite source model; 1999 Athens earthquake; 1997 Kagoshima earthquake

Introduction

Strong ground motion seismology plays a key role in mitigating possible damage caused by earthquakes in active regions. Seismic engineers need, as an input, broadband (0 – 20 Hz) synthetic seismograms at small (< 100 km) source distances. Simulation techniques that provide such data have to take into account finite-extent source models to characterize the key features of ground motions from large earthquakes (e.g., source directivity).

There are various kinematic approaches to the representation of the rupture processes on an extended fault (*Hartzell et al.*, 1999). The approaches can be divided into four groups:

Integral. In this approach one prescribes the main kinematic properties of the fault, which would generate the widely observed ω -squared spectrum (*Andrews*, 1980 and 1981, *Bernard et al.*, 1996, *Gallovič and Brokešová*, 2004). The radiated wavefield is then simply calculated using the integral in the representation theorem, which requires the computation of Green’s functions in a relatively dense grid of points over the fault.

Composite. The source process is represented by relatively few segments, so-called subevents or subsources. Each subsurface is characterized by its source time function (or its parameters, such as the seismic moment, corner frequency, etc.) Contributions of subevents are summed and the resulting wavefield is filtered in order to obtain the proper seismic moment and spectral shape of the source function corresponding to the whole earthquake. This approach often utilizes the Empirical Green’s Function (EGF) method where an aftershock is taken as the record of the small rupture, but the analytic Green’s function can be used as well. More about composite modeling can be found in the papers by *Frankel* (1991), *Irikura and Kamae* (1994), *Zeng et al.* (1994) and others.

Stochastic. One directly prescribes an envelope of the modeled seismogram to correspond to a given earthquake (in terms of, e.g., seismic moment, corner frequency, duration, etc.). The high frequencies are then generated in a purely stochastic way, for example, as white noise (*Boore*, 1983). The main problem is that this modeling approach has nearly no physical background so that we do not consider it here.

Hybrid combination of the above approaches. This combination can be constructed in various ways (*Beresnev and Atkinson*, 1997, *Pacor et al.*, 2005, etc.). Some of the methods (e.g., *Hartzell et al.*, 1999 and 2005) utilize integral and composite approaches for low frequency and high frequency bands, respectively. However, in previous studies the integral and composite models in the hybrid approach are unrelated, which can lead to improper spectral matching in the cross-over frequency zone. The aim of this paper is to propose a hybrid model with related low- and high-frequency models.

Let us start with a relatively simple, integral, kinematic, finite-extent source model as used by *Gallovič and Brokešová* (2004). The source is represented

by a rectangular fault, along which a radial rupture front propagates from a nucleation point at a constant velocity. At a point through which the rupture front passes, a slip starts to evolve during a time interval equal to rise time τ . At time τ the slip reaches its maximum value and then remains constant. The final (maximum) slip varies along the fault and has a k -squared distribution (*Bernard and Herrero, 1994, Gallovič and Brokešová, 2004*). This means that the decay of the slip wave-number amplitude spectrum is proportional to k^{-2} (k being the radial wave number) for large wave numbers and its phase is random. It can be shown (*Gallovič and Brokešová, 2004*) that such a slip distribution results in desirable ω -squared source spectrum provided that rise time τ is wave-number dependent. More specifically, $\tau = \tau_{max}$ is constant up to a certain wave-number k_0 and then decreases linearly with increasing $k > k_0$ (for details see *Bernard et al., 1996* and *Gallovič and Brokešová, 2004*). At a given time, faulting thus appears in a strip bounded by the rupture front on one side and by the healing front (given by the maximum rise time τ_{max}) on the other side. Thus, the rupture propagates along the fault in the form of a slip pulse (*Heaton, 1990*).

Strong ground motions, generated by such a source model, are calculated according to the representation theorem by computing the well-known surface representation integral along the fault. Assume a rupture described by pure shear dislocation $\Delta\mathbf{u}(t, \boldsymbol{\xi})$ along fault Σ , t and $\boldsymbol{\xi}$ being the time and the position along the fault, respectively. For a receiver at position \mathbf{r} , the representation theorem reads (e.g., *Aki and Richards, 2002*)

$$u_i(\mathbf{r}, t) = \iint_{\Sigma} G_{ip,q}(\mathbf{r}, t, \boldsymbol{\xi}) * m_{pq}(t, \boldsymbol{\xi}) d\Sigma(\boldsymbol{\xi}), \quad (1)$$

$$m_{pq}(t, \boldsymbol{\xi}) = \mu (\nu_p \Delta u_q(t, \boldsymbol{\xi}) + \nu_q \Delta u_p(t, \boldsymbol{\xi})) \quad (2)$$

where u_i is the i -th component of ground displacement, $\boldsymbol{\nu}$ the unit normal to the fault. Quantities \mathbf{G} and \mathbf{m} are Green's tensor and moment tensor density, respectively. The comma in the suffix indicates the spatial partial derivative with respect to $\boldsymbol{\xi}$ (i.e. $G_{ip,q} = \partial G_{ip} / \partial \xi_q$) and $*$ denotes time convolution. The k -dependent rise time is introduced in $\Delta\mathbf{u}(t, \boldsymbol{\xi})$ (Eq. (2)) by means of the formula introduced in *Gallovič and Brokešová (2004)*.

Numerically, the fault is discretized, and the representation integral is replaced by a sum, so that the finite extent source is represented as a superposition of point sources distributed regularly along the fault with the spacing small enough to avoid numerical problems in the integral evaluation. It is clear that this procedure could require a large numerical effort for high frequencies due to the necessity of a dense fault discretization.

On large scales (i.e. large spatial wavelengths), the source model explained above is acceptable since it is assumed that the faulting process can be described deterministically. This is also supported by the low-frequency slip inversions (e.g., *Hartzell and Heaton, 1986, Wald et al., 1996, Asano et al., 2005*). On

the other hand, although the model seems to be complicated in terms of the stochastic component in the slip phase spectrum at small wavelengths (*Herrero and Bernard, 1994*), it is likely too simple to represent actual source behavior at small wavelengths. Due to the presumably heterogeneous distribution of dynamic and geometric rupture parameters on small scales, the rupture is expected to be disorganized (chaotic, being a non-linear and incoherent process). Consequently, the integral description may not be well justified from the physical point of view on low scales. Moreover, the integral approach may become numerically too expensive when computing up to high frequencies. Note that the relative simplicity of the integral k -squared rupture model (in terms of homogeneous rupture propagation) can contribute significantly to a strong directivity effect, which is hardly observed especially at high frequencies (*Joyner, 1991, Bernard et al., 1996, Gallovič and Burjánek, 2006*).

Andrews (1981) has developed a complex integral stochastic model that includes the chaotic short-scale rupture evolution. A possibly more practical approach (simply tractable and computationally more efficient) is to utilize the composite model, in which the source acts as a discrete sequence of individually rupturing subevents. This approach has to be understood as a phenomenological source representation describing average source behavior¹. Note that the composite approach has been successfully applied in the high-frequency modeling of ground motions (*Irikura and Kamae, 1994, Frankel, A., 1995, Roumelioti et al., 2004, etc.*). Regarding long spatial wavelengths (where the source behavior is rather deterministic), the composite approach does not take into account spatial variations of Green's functions over a given subsurface when evaluating low-frequency ground motions. Moreover, most of the composite techniques require artificial filtering in order to enhance the low-frequency content of the synthetics (to match the seismic moment of the modeled event, e.g., *Frankel, 1995*). Consequently, the composite methods do not correctly model the coherent low-frequency pulses that may control the period, duration, and amplitude of near-fault ground motions at frequencies shorter than about 1 sec.

Let us summarize: while the integral approach is more suitable for short-scale source description (correctly modeling possible low-frequency ground motions), the composite model represents the short-scale source behavior better (being numerically effective and successful in modeling high-frequency seismograms). To retain the advantages of both the methods, we propose a new, hybrid k -squared, kinematic, finite-extent source model applicable on both large and small scales, providing a ω -squared source spectrum. The subsources in the composite part are constrained to provide a spatial slip amplitude spectrum decaying as k^{-2} for large k 's (similarly to the integral model explained above).

¹The composite approach can also be understood to incorporate (in addition to the complex source effects) short-wavelength effects of complex wave propagation as well, so that even in high-frequency computations relatively simple Green's functions can be employed instead of much more complex ones.

Source description – key ideas

In the hybrid model presented, we decompose the faulting process into slipping on individual, virtual, overlapping subsources of various sizes, distributed randomly along the fault. A similar decomposition is inherent to the composite approaches (see, e.g., *Hartzell, 1978, Irikura and Kamae, 1994, Zeng et al., 1994, Frankel, 1995, Beresnev and Atkinson, 1997*). However, in our hybrid model the same set of subsources is used even in the integral calculations. The specific computational realization of the set of subsources is different in previous studies (rectangular, circular, overlapping, non-overlapping, etc.) These features follow from the adopted source model concept. In our hybrid k -squared source model, the assumption of the k -squared slip distribution along the fault is essential, implying the relation between the subsources' mean slips and their number-size distribution. *Andrews (1980)* has shown that subsources with a number-size distribution described by a power law with fractal dimension $D = 2$ and with mean slips proportional to their dimensions (so-called constant stress-drop scaling) compose the desired k -squared slip distribution. Note that *Zeng et al. (1994)* assumed the same scaling properties of the subsources, however, the authors did not take advantage of this consequence. It is intrinsically assumed that the source model is self-similar in that sense that the individual subsources are also, like the whole fault, composed of smaller subsources having thus also the k -squared slip distribution. We do not simulate this explicitly (by summing "subsubsource" slip contributions), we only directly prescribe a k -squared slip distribution for each of the individual subsources.

We assume that the subsources contribute differently to the wavefield at different spatial wavelengths. On large scales, the subsources (of all dimensions) act so that the fault motion is equivalent to the integral k -squared model discussed above. The final slip at a point on the fault is given by the sum of the slip contributions from the individual subsources overlying the point. The subsources compose rupture propagating at a constant velocity over the whole fault and the slip increases with a given (k -dependent) rise time, so that the rupture process is concentrated in a slip pulse of constant width propagating at a constant rupture velocity along the fault. The generated wavefield is (by definition) the same as that of the integral k -squared model in which the contributions from different source points along the fault sum coherently.

On small scales, the situation is different. The behavior of subsources is assumed to be chaotic. The rupture process is likely too complicated to be describable by a relatively simple space-time distribution of slip function $\Delta \mathbf{u}$ (e.g., by the use of a single distinguished rupture front). An intuitive idea of such source behavior on small scales can be gained from the snapshot illustrating the slip velocity field in Fig. 1. Instead of attempting to simulate the particular subsource behavior, which may be rather complex, we assume that the radiated high-frequency wavefield $\mathbf{u}_s^{HF}(\mathbf{r}, t)$ of a given subsource s can be effectively ap-

proximated by

$$\mathbf{u}_s^{HF}(\mathbf{r}, t) = \mathbf{C}(\mathbf{r}, t, \boldsymbol{\xi}_s) * \Omega_s(t) \quad (3)$$

$$\Omega_s(t) = \iint_{\Sigma_s} \Delta \dot{u}_s(t, \boldsymbol{\xi}) d\boldsymbol{\xi}, \quad (4)$$

where \mathbf{C} comprises the propagation effects and radiation pattern, $\boldsymbol{\xi}_s$ denotes a given point in the subsurface (usually its center) and Σ_s is the subsurface's surface. We call $\Omega_s(t)$ the source time function. Slip rate function $\Delta \dot{u}_s$ describes the partial evolution of the rupture on the given subsurface. Being presumably complex and disorganized, evolving chaotically in all directions, we can assume that, effectively, the radiation of the high-frequency wavefield is isotropic and that its origin is point $\boldsymbol{\xi}_s$ on the subsurface. Thus, the resulting source time function of the individual subsurface is independent of the receiver position and, consequently, the directivity effect vanishes. In this way, the subsurfaces act as individual point subevents and they are equivalent to randomly distributed point sources (as in the composite approach). Note that due to the random subsurface position, the subsurfaces' wave-field contributions sum incoherently. In the composite part of the hybrid model we prescribe directly $\Omega_s(t)$, characterized by seismic moment m_s and corner frequency f_s^c of a given subsurface s . More specifically, in this paper, we assume Brune's source time function which, in the spectral domain, reads

$$\Omega_s(f) = \frac{m_s}{(1 + if/f_s^c)^2}, \quad (5)$$

where the symbol i represents the imaginary unit. The choice of quantities m_s and f_s^c is discussed in the next section.

Let us discuss briefly the spatial wavelength dividing the deterministic and chaotic description of the rupture and its relation to the slip pulse width. Beroza and Mikumo (1996) address the presence of the slip pulse to the dynamic stress drop heterogeneity. Whatever the cause of the stress drop heterogeneity, in the source model it introduces characteristic length scales much smaller than the overall dimensions of the fault, which in turn leads to relatively narrow slip pulses. We suppose that the same dynamic process causes the rupture to become chaotic on small scales. Consequently, the slip pulse width should be somehow related to the spatial wavelength dividing the deterministic and chaotic description of the rupture. A more profound analysis of this phenomenon is beyond the scope of the present paper. For simplicity, we assume that the slip pulse width is about the same as the dividing wavelength. However, note that this assumption is only tentative. If future studies show that the two spatial wavelengths are different, the hybrid k -squared model will still hold after a straightforward modification.

Computational realization of the source model

Before starting computations it is necessary to develop a subsource database, which includes their positions along the fault, dimensions, mean slips (and consequently seismic moments) and corner frequencies. Let the fault be a rectangle of dimensions $L \times W$. Subsource dimensions are taken as integer fractions of L and W , i.e. the subsource length is $l_n = L/n$ and its width is $w_n = W/n$. Henceforth, we call the integer n the subsource level. The levels range from n_{min} to n_{max} . At each level all subsources are assumed to be identical in dimensions, mean slip and corner frequency, while their position is generally random (with possible exceptions at the lowest levels, see below).

The database is developed in the following way:

- The number of all the subsources at levels $\leq n$, i.e. of size $l_n \times w_n$ and larger, is n^2 (given by the assumed fractal dimension $D = 2$ of the number-size distribution). More specifically, the number of subsources $N(n)$ at level n can be obtained as the difference between the number of all the subsources up to level n and up to level $n - 1$, i.e. $N(n) = n^2 - (n - 1)^2 = 2n - 1$. The subsource at level 1 corresponds to the whole fault.
- The positions of the subsources are assigned generally randomly (the subsources may overlap) unless constraints, if any, apply. For example, the evidence of clear asperity in the slip inversion result may constrain the positions of the lowest-level subsources to be fixed.
- The mean slip for the subsources at level n is given by $\Delta \bar{u}_n = c_u/n$ (obtained from the constant stress-drop assumption). In this way, the average slip is proportional to the subsource dimension. The constant of proportionality c_u , assumed to be independent of n , is obtained by matching the seismic moment of the whole earthquake to the sum of the moments of all the subsources at levels from n_{min} to n_{max} .
- The corner frequencies f_n^c of the subsources at level n are considered to be inversely proportional to the subsource dimension (and, consequently, the subsource duration), i.e. $f_n^c = c_f n$. The reciprocal of c_f , considered independent of n , is comparable to the duration of the whole earthquake. There are several ways of constraining the value of c_f . It can be found, for example, by comparing the synthetic PGAs with the local attenuation relations (see numerical examples) since f_n^c controls the high-frequency spectral level of the synthetics. Alternatively, if the attenuation relations are not available and the aim is to model observed data, c_f can be estimated as the reciprocal of the event duration and then adjusted by comparison with observed seismograms. If the aim is prediction of a future event and there are no attenuation relations for the area under study, c_f can be set up by

constraining the high-frequency spectral level of the whole earthquake (assuming incoherent summation of the subsources' contributions) by means of an empirical relation between the corner frequency and the earthquake magnitude. Note that, if even this relation is unknown, the empirical relation can be substituted by the relation following from a considered dynamic model, e.g., Brune's model (*Brune, 1970*).

We use two methods for strong motion synthesis in two different frequency ranges. Let us assume two bounding frequencies f_1 , f_2 , with $f_1 < f_2$. For frequencies up to f_2 we use the integral approach and for frequencies larger than f_1 the composite approach. In order to simulate smooth transition between the deterministic and chaotic style of faulting, we combine the computed synthetics in the Fourier domain in the cross-over frequency range between frequencies f_1 and f_2 , as illustrated in Fig. 2. For both the real and imaginary parts of the spectrum, we apply weighted averaging by using the $\sin^2(x)$ and $\cos^2(x)$ weighting functions, where $x = \frac{\pi}{2} \frac{f-f_1}{f_2-f_1}$ (see also *Mai and Beroza, 2003*). Frequencies f_1 and f_2 are in fact free parameters making the hybrid model as general (robust) as possible. The choice of f_1 and f_2 is discussed in the section Numerical examples.

Concerning the low-frequency (up to f_2) computation according to the representation theorem (Eq. (1)), we discretize the fault densely enough to compute the integral correctly up to frequency f_2 . The static slip at a point is given by the sum of static slips of all the subsources from the database that contain the point (assuming generally k -squared slip distribution on each individual subsource, see above). An example of the slip distribution constructed in this way is shown in Fig. 3. The figure also shows that the proposed procedure provides a k -squared slip model. The rupture time is given by the distance of the point from the nucleation point assuming constant rupture velocity v_r . Slip velocity function Δu is assumed to be Brune's pulse, with, generally, k -dependent rise time τ . The spectrum of the pulse has the same form as that in Eq. (5), where $\Omega_s(f)$, m_s and f_s^c are to be replaced by $\Delta u(f)$, mean slip and $1/\tau$, respectively. Note that the maximum rise time τ_{max} defines the slip pulse width as $L_0 = v_r \tau_{max}$. In certain cases, if $1/\tau_{max}$ falls in the cross-over frequency range, the rise time can be specified as constant.

In the high-frequency range (above f_1), the composite approach is utilized. The subsources from the database are treated as point sources (Eq. (3)) with Brune's source time functions (Eq. (5)), approximating the average radiation from the subevents rupturing rather chaotically (see above). The subsources' seismic moments and corner frequencies are obtained directly from the database. The rupture time is given by the time the rupture takes to reach the subsource's center (assuming the same constant velocity v_r as for the integral approach).

The introduced source model can be combined with any method providing Green's function. In this paper we use the ray theory (more precisely direct S-waves only) and the discrete wave-numbers method (*Bouchon, 1981*).

Numerical examples

Athens earthquake

The hybrid approach described above is used for modeling the PGAs generated by the 1999 Athens earthquake. The results from the hybrid model are compared to those obtained by the purely integral k -squared rupture model (with k -dependent rise time) and the purely composite model. The models share the same subsource database in order to compare their results properly. Since this earthquake is predominantly unilateral, we can expect different results from the two models implied by different amounts of directivity at high-frequencies.

The basic parameters of the Athens earthquake model are based on previous studies (*Tselentis and Zahradník, 2000, Roumelioti et al., 2003*). They are listed in Tab. 1. For the earthquake location and mechanism see Fig. 4. We assume that the rupture propagates radially at constant rupture velocity v_r from a nucleation point that corresponds to the hypocenter given by NOA: 38.08° N and 23.58° E. The maximum rise time is equal to 1 sec in both the hybrid and purely integral model.

The slip model is based on the inversion result by *Roumelioti et al. (2003)*. By visual inspection one can characterize it by two asperities (one of a high and the other of a low slip contrast), see Fig. 5. Both are located in the left part of the fault, the high- and low-contrast asperity being situated down- and up-dip from the hypocenter, respectively. To account for such a particular slip (subevent) distribution, we neglect the subsource at level $n = 1$ that would be of the dimension of the whole fault. The three subsources at level $n = 2$ are placed to the left of the fault (two of them at the top and one at the bottom) to simulate the asperities. An example of one realization of such slip distribution is shown in Fig. 3. The corresponding slip contrasts of the high- and low-contrast asperities are, approximately, 2x and 1x the mean slip of the whole earthquake model, respectively.

Let us discuss the choice of bounding frequencies f_1 and f_2 . According to our tentative assumption that the slip pulse width and wavelength dividing the deterministic/chaotic rupture behavior are about the same (see above), the cross-over interval should be spread around the so-called dividing frequency, being equal to the reciprocal of the rise time (i.e. 1 Hz in our case). Another practical assumption (not based on the tentative consideration) may be, for example, that the dividing frequency equals the highest frequency used to obtain reliable results in kinematic slip inversions (utilizing implicitly the integral approach). In the case of the Athens earthquake slip inversion by *Roumelioti et al. (2003)*, the highest frequency is (also) 1 Hz. Regarding the width of the cross-over range (i.e. f_1 and f_2), we define it, to advantage, relatively to the dividing frequency by a multiplicative factor (note that this choice is user-dependent). Our particular choice of the factor of 2 (i.e. $f_1 = 0.5$ Hz and $f_2 = 2$ Hz) is based on our experience

that this range is large enough not to result in a significant step between the low- and high-frequency spectral levels on the log-log plot. Based on our numerical testing, slight changes of these frequencies do not affect the results considerably.

We consider the crustal model, called MA, used in modeling of the regional data by *Tselentis and Zahradník* (2000). This 1D structural model consists of the homogeneous layers described in Tab. 2. The uppermost 1 km low-velocity layer is partly confirmed by, e.g., the surface waves dispersion study (see *Novotný et al.*, 2001).

Green’s functions are computed using the standard ray theory (*Červený*, 2001). In this part, we restrict the computations to direct S waves only since they are considered to be dominant for PGAs at epicentral distances of our interest (< 30 km). This restriction is quite common in many papers (e.g., *Hanks*, 1982, *Zollo et al.*, 1997, *Emolo and Zollo*, 2001 and 2005).

The computer code for 2D ray computations BEAM87, written by *Červený* and modified by *Brokešová* (1993) to allow for 2.5D computations, is used. Under the 2.5D computation we understand computation of 3D rays in a 2D medium (i.e. a medium with properties dependent on the vertical and one horizontal coordinate). Note that in the 1D medium considered in this study the rays are, in fact, in-plane, which implies more efficient two-point ray tracing. Nevertheless, due to the ”arbitrary” source-receiver configuration, the problem is 3D. Moreover, the extension to 2D structures would be straightforward. For faster computations, the quantities determining each S-wave (arrival time, real and imaginary part of its amplitude) are interpolated using bicubic splines, since their changes with respect to the position along the fault are smooth in our particular crustal model.

The synthetics are band-pass filtered between 0.5 and 10 Hz. The attenuation effects are approximated by frequency-dependent quality factor $Q(f) = 100 * f^{0.8}$ as used also by *Roumelioti et al.* (2004). The effect of the near-surface attenuation was also taken into account by diminishing the simulated spectra by the factor $\exp(-\pi\kappa f)$ (*Anderson and Hough*, 1984), where $\kappa = 0.01$ sec as a typical value for rock sites. No other site effects or topography are taken into account.

As suggested above, we adjust parameter c_f (for hybrid and purely composite models) by comparing synthetic horizontal PGAs (maximum of the horizontal components) with the empirical attenuation curve for Greece (*Skarlatoudis et al.*, 2003). Fig. 6 shows PGAs plotted as a function of epicentral distance, simulated by the hybrid method assuming various values of c_f . Synthetics are calculated for 112 virtual receivers, spaced regularly every 4 km along 16 profiles running radially from the epicenter (Fig. 7, top). One can see that c_f predominantly affects the overall level of the PGA values, while the scatter remains nearly unchanged. The best correspondence with the attenuation curve is for $c_f = 1/4 \text{ s}^{-1}$ when all the simulated PGA values fall within the empirical $\pm 2\sigma$ uncertainty bounds.

Fig. 7 (top) shows the mean horizontal PGAs obtained by the use of the three models from 10 different slip realizations (or, equivalently, distributions of subsources), with the asperity locations and nucleation point position fixed. At

the bottom of Fig. 7, all the synthetic PGAs are gathered and plotted versus epicentral distance and compared with the attenuation curve published by *Skarlatoudis et al.* (2003). The attenuation relations provide not only mean values, but also a measure of their uncertainty (standard deviation σ). The scatter in the published attenuation relations is caused by, e.g., 3D structural effects, including site effects, and also by the directivity and radiation-pattern effects varying with receiver azimuth. We assume that 2σ above and below the mean empirical attenuation curve represent an upper and lower bound, respectively, for the synthetic PGAs. In Fig. 7 (bottom) we can see that, in the hybrid (and composite) method, the synthetic PGAs are distributed around the mean attenuation curve and that their scatter is lower than 2σ around the empirical mean. The integral k -squared method has a larger scatter because of the low PGAs at anti-directive receivers (see Fig. 7 (top)). The strong directivity effect is caused by the coherent summation of contributions from the individual point sources even at high frequencies, while the hybrid (composite) approach yields weaker directivity due to the incoherent summation of the subsources' wavefield contributions.

For illustration, Fig. 8 shows, for 2 selected stations (both 24 km from the epicenter, one in the forward and one in the backward direction with respect to the rupture propagation, see Fig. 7 for their positions), a comparison of synthetic seismograms (displacement, velocity and acceleration) obtained by the three discussed methods: purely integral, purely composite and their hybrid combination. In the forward directivity zone, one can see that the displacements (with predominantly low-frequency spectral content) obtained by the three methods are nearly the same. On the other hand, at the backward-direction station the purely composite method yields a narrower pulse with a different amplitude than the other two methods. This, in consequence, means that this method would not be able to reproduce correctly the low-frequency directivity effect. With respect to accelerations (with dominant high-frequency content), the composite method provides the same waveforms as the hybrid one at both stations. Note that the directivity effect is very small, in contrast to the result given by the purely integral model, which is due to different summations (coherent/incoherent) of the wavefield contributions from the individual subsources. In synthetic velocities, the spectral content at frequencies around the corner frequency plays a dominant role. In our example, this region coincides more or less with the cross-over zone, so that all the three synthetic waveforms differ significantly from one another, especially at the backward-direction station. Comparing the absolute PGV values for the two stations, we can see that the strongest directivity effect is provided by the integral approach while the weakest by the composite model. Note that the differences are also affected by the choice of the cross-over frequency range. Although f_1 coincides with the high-pass filtering frequency (0.5 Hz), the integral part still plays an important role especially in the first half of the relatively broad cross-over zone. If the high-pass filtering frequency is lower (< 0.5 Hz), the synthetics may differ more significantly from one another.

To show that the hybrid Athens earthquake model is realistic and capable of reproducing observed strong ground motion data, Fig. 9 compares the synthetic and observed accelerations for the transverse component at station DMK (see Fig. 7 for its position). The station was selected as the only one installed on hard rock that can be considered "free-field" (*Roumelioti et al.*, 2004). The transverse component is assumed to be affected mainly by the SH waves that are involved in our synthetics. As one can see, the synthetic waveforms vary considerably for different realizations of the subsurface distribution although the asperities position is fixed. Nevertheless, their overall appearance agrees well with the observed data in terms of complexity, major peaks and frequency content. In this sense, the hybrid model is supported by the observation.

Kagoshima earthquake

In this example we demonstrate the application of the hybrid approach to the March 1997 Kagoshima earthquake ($M_w = 6.1$), Kyushu, southern Japan. The earthquake location and mechanism are taken from *Horikawa* (2001), see Fig. 10. The results are compared with the observed velocigrams recorded by the K-NET and JMA stations. We restrict our study to 20 stations at relatively short epicentral distances, less than 50 km, see Fig. 10. The records are band-pass filtered between 0.2 – 10 Hz.

The Kagoshima earthquake was extensively studied by *Horikawa* (2001). The main features of the earthquake are adopted from that paper (see Tab. 1). *Horikawa* fixed the nucleation point position in the middle of the strike direction and at 1/3 of the fault depth range from the bottom. He then found the relative position of the asperity in the bottom west part of the fault by fitting low-frequency waveforms using a simple kinematic model. We take the asperity into account in a similar way (by constraining the position of the largest subsources) as in the case of the Athens earthquake (see above). We fix both asperity and nucleation point positions in our computations.

We adopt the crustal model used by *Horikawa* (2001), see Tab. 3. Green's functions are computed using the discrete wave-numbers technique (*Bouchon*, 1981) for the whole frequency range, so that we obtain the complete wavefield. For faster computations, interpolation in the frequency domain (of real and imaginary parts separately) is applied (*Spudich and Archuleta*, 1987).

The choice of the transition frequency zone $f_1 = 0.5$ Hz and $f_2 = 2$ Hz (the same as in the previous example) appears to be suitable for this case as well. Parameter $c_f = 1/3$ s⁻¹ is set in order to get general agreement between the modeled PGA and PGV values and attenuation curves for Japan (*Si and Midorikawa*, 1999). Fig. 11 shows the simulated peak values for 5 slip realizations (open circles) plotted together with the attenuation curve and its uncertainties. Moreover, the observed PGAs and PGVs are shown (gray circles) to support the use of the attenuation relation when adjusting c_f . However, the aim of Fig. 11 is

not in providing a detailed comparison of peak values at the individual stations. Such a comparison would require a site-specific treatment.

We assume (similarly to the case of the Athens earthquake) 5 realizations of the slip (subsources) distribution. The synthetics are band-pass filtered in the same way as the real records (0.2 – 10 Hz). For several selected stations (gray-marked in Fig. 10), Fig. 12 shows the comparison between the observed horizontal velocigrams and all of the 5 corresponding synthetics both in the time and frequency domains. The stations are selected by visual inspections with the aim to choose those characterized by a duration comparable with the duration of the synthetics, i.e. the stations supposedly not being affected much by complex propagation/site effects (which are not taken into account in our Green’s functions). For illustration, this requirement was deliberately disregarded in the case of station KGS008. The velocigrams in the time domain are normalized, so that one can compare peak values (numbers in the figure) and waveform shapes separately.

The synthetics reproduce the complexity of measured waveforms relatively well. At stations KGS001, KGS003, KGS005 and KMM015, the match between synthetic and observed data is very good in terms of basic shape of the waveform, duration of the most significant wavegroups, polarity, spectral level and the spectral decay. For certain stations (or components) there is a discrepancy between the synthetic and observed spectral levels in the range from 0.2 to about 0.5 Hz. However, this discrepancy does not probably contradict the waveform fitting by *Horikawa* (2001) whose inversion relies on lower frequencies (0.1 – 0.2 Hz). Note that at station KMM015 one can see a very good fit of relatively complex shape of the observed Fourier spectrum, although it does not have a simple ω -squared shape. At stations KGS001 and KGS005 synthetic and observed peak values are about the same, while at KGS003 and KMM015 they differ by a factor of about 2. In Fig. 10, one can see that these stations are located around the source at various azimuths and distances of 10 – 30 km.

At station KGS002 the overall shapes (envelope, duration) of the synthetic and observed records are in good agreement. The synthetic and observed spectra fit each other well up to about 4 Hz, but for higher frequencies the synthetic spectra decay considerably faster. This could possibly be caused by high-frequency site and/or propagation effects. A similar, but much more pronounced discrepancy in the behavior of the high-frequency spectrum can be seen in the case of station KMM018 to which the waves propagate partly through sea water (see Fig. 10). At station KGS004, the real data and synthetics are in relatively good agreement in the time domain. In the frequency domain, there is a remarkable amplification in the observed spectra at frequencies between about 0.3–1.5 Hz, not reproduced in the synthetics. We attribute this to a possible resonant site-effect not included in our computation. Moreover, beyond the resonant amplification, the synthetic spectral amplitudes are higher than the observed ones. At station KGS008 (Fig. 12) strong site-effects are clearly seen in the time domain. They are manifested

mainly by the longer duration of the observed waveforms with a prevailing frequency of about 1 Hz. In the frequency domain this feature is manifested by higher observed spectral amplitudes around 1 Hz. At frequencies higher than 1 Hz, the agreement between observed and synthetic amplitude spectra is again good.

Discussion and conclusions

We present a hybrid source model composed of individual overlapping subsources distributed randomly along the fault. In general, this model is suitable for both integral and composite source descriptions. The spatial wavelength dividing these two source representations is, in general, a subject of choice. We hypothesize that the realistic choice of the dividing wavelength is comparable to the slip pulse width. This assumption has to be justified by advanced source studies (dynamic, experimental, etc.) and/or systematic modeling of strong ground motion data. Nevertheless, if such studies show that the dividing wavelength and the slip pulse width differ considerably, the hybrid k -squared model will still be applicable, only frequencies f_1 and f_2 will have to be chosen accordingly. Note that it is also possible to set the dividing wavelength equal to the maximum wavelength considered, thus obtaining a purely composite approach, very similar to the model of *Zeng et al.* (1994). On the other hand, setting the dividing wavelength equal to the minimum wavelength, one obtains a purely integral model that is equivalent to the kinematic k -squared model of *Bernard et al.* (1996) and *Gallovič and Brokešová* (2004) if combined with a k -dependent rise time. We should emphasize that the desirable ω -squared source spectrum is obtained in any case.

Let us discuss what our proposed model implies for slip velocity functions over the fault. In the hybrid model, their spectral content can be divided into two ranges. At large wavelengths (and, consequently, low frequencies) their shape is deterministic (i.e. relatively smooth), given by the propagating slip pulse. At small wavelengths (high frequencies) their shape is perturbed by stochastic contributions from the chaotic faulting style. The construction of such slip velocity functions is left to future studies. However, we expect they would mimic those introduced by *Andrews* (1981).

Our modeling results for the particular case of the 1999 Athens earthquake show that the hybrid approach predicts directivity in correspondence with observation (attenuation relations) in terms of the PGA scatter. The second example, the 1997 Kagoshima earthquake, shows that, despite the neglected site-effects, the model reproduces the complexity of measured waveforms relatively well. Note that in the presented numerical examples information from kinematic slip inversions (defining the positions of asperities) is used in order to constrain the low-frequency part of the spectrum. In certain applications (simulations for hypothetical earthquakes, scenario studies) such information may not be available. In such situations one can leave the subsources at level 2 random. Note that in

our particular examples the transition between integral and composite modeling in the cross-over frequency zone is not pronounced in the synthetic spectra, or in the time domain.

The separation of the computation into two parts allows different techniques to be used in computing Green's function in both frequency ranges. For example, finite differences or finite elements can be used for low-frequency (integral) calculations and stochastic Green's functions for the high-frequency (composite) part of the wavefield. We assume that, since both the integral and composite approaches are based on the same, properly scaled set of subsources, the cross-over filtering of low and high frequency spectral amplitudes in the transition zone (see Fig. 2) will not introduce any artificial behavior of the synthetic waveforms.

Let us discuss our assumption of the rupture velocity and rise time in the integral part of the hybrid model. For simplicity, both of them are considered constant in our study. However, they can be, in general, prescribed variable, e.g., in agreement with slip inversion results, and/or to be consistent with source dynamics as suggested by *Guatteri et al.* (2004). This would better constrain the integral part of the simulated wavefield. On the other hand, we do not expect that the variable rupture velocity would change the composite part of the synthetics substantially because of the incoherent summation, which is, by definition, insensitive to rupture time variations. The shape of the slip velocity function in the integral part of the model can, in principle, be chosen in any suitable form. In our examples, the choice of Brune's function seems to be sufficient. When required, it can be chosen, e.g., in a more "dynamically compatible" form, such as *Kostrov's* (1964) function. Note that if the reciprocal of the slip function duration falls within the cross-over frequency range, the details of its shape will play a rather minor role in the synthetics.

We have applied the hybrid k -squared model to medium-size earthquakes ($M_w=5.9$ and $M_w=6.1$), for which the fault length-to-width ratio is not very large (which holds for the subsources as well, since they are constructed as fractions of the entire fault). For larger events, the fault length-to-width ratio may be very large (say $L/W > 4$, *Wells and Coppersmith*, 1994). Consequently, the subsources constituting the final slip are elongated. Indeed, elongated slip patches are sometimes observed in kinematic slip inversions of past earthquakes, e.g., 1979 Imperial Valley (*Hartzell and Heaton*, 1986), 1999 Hector Mine (*Ji et al.*, 2002), 2002 Denali (*Asano et al.*, 2005). On the other hand, inverted slip distributions of some other earthquakes are characterized by rather symmetrical (quasi circular) slip patches, e.g., 1989 Loma Prieta (*Emolo and Zollo*, 2005), 1992 Landers (*Wald and Heaton*, 1994). In such cases, square or circular subsources should be used instead of rectangular ones, suggested in this work. Their maximum size would have to be constrained by the width of the fault. However, such a modification of the hybrid model has not been tested yet and is left to future studies.

Finally, let us summarize the advantages of the hybrid model:

- Contrary to the integral k -squared approach, chaotic small-scale behavior is involved. It results in a more realistic directivity effect.
- Contrary to the composite approach, the model is better constrained for low-frequency calculation, e.g., for slip inversions (no artificial low-frequency filtering is necessary).
- The combination of the integral and composite approaches is numerically efficient with respect to the purely integral one.

Acknowledgement

The authors benefited from discussions with Jan Burjánek. Martin Mai and Antonio Emolo provided invaluable comments that helped to improve the manuscript. The research was financially supported by Grant Agency of Charles University (292/2005/B-GEO/MFF), Marie Curie training network SPICE in the 6th Framework Program of the European Commission (MRTN-CT-2003-504267) and by Italian National Institute of Geophysics and Volcanology and of the Italian Civil Defence Department.

References

- Anderson, J. G., Hough, S. E. (1984). A model for the shape of the Fourier amplitude spectrum of acceleration at high frequencies, *Bull. Seism. Soc. Am.* *74*, 1969-1993.
- Andrews, D. J. (1980). A stochastic fault model, 1. Static case, *J. Geophys. Res.*, *85*, 3867–3877.
- Andrews, D. J. (1981). A Stochastic Fault Model, 2, Time-dependent Case, *Journal of Geophysical Research* *86*, 10821–10834.
- Aki, K., Richards, P.G. (2002). *Quantitative Seismology*, 2nd Edition, University Science Books., Sausalito, CA. 700 pp.
- Asano, K., Iwata, T., Irikura, K. (2005). Estimation of source rupture process and strong ground motion simulation of the 2002 Denali, Alaska, earthquake, *Bull. Seism. Soc. Am.* *95*, 1701–1715.
- Beresnev, I. A., Atkinson, G.M. (1997). Modeling finite-fault radiation from the ω^{-n} spectrum, *Bull. Seism. Soc. Am.*, *87*, 67-84.
- Bernard, P., and A. Herrero (1994), Slip heterogeneity, body-wave spectra, and directivity of earthquake ruptures, *Annali di Geofisica*, Vol. XXXVII, 1679-1690.
- Bernard, P., A. Herrero, and C. Berge (1996), Modeling directivity of heterogeneous earthquake ruptures, *Bull. Seism. Soc. Am.* *86*, 1149-1160.
- Beroza, G., and T. Mikumo (1996). Short slip duration in dynamic rupture in the presence of heterogeneous fault properties, *J. Geophys. Res.* *101*, 22,449-22,460.

- Boore, D.M. (1983). Stochastic simulation of high-frequency ground motions based on seismological models of the radiated spectra, *Bull. Seism. Soc. Am.* **73**, 1865–1894.
- Bouchon, M. (1981). A simple method to calculate Green's functions for elastic layered media, *Bull. Seism. Soc. Am.* **71**, 959–971.
- Brokešová, J., 1993, *High-frequency ground motions due to extended seismic sources in complex structures*, PhD. Thesis, Charles University, Prague.
- Brune J., 1970. Tectonic stress and the spectra of seismic shear waves from earthquakes. *J. Geophys. Res.*, **75**, 4997-5009. (correction, *J. Geophys. Res.*, **76**, 5002, 1971).
- Červený, V. (2001). Seismic Ray Theory. *Cambridge University Press*.
- Emolo, A., Zollo, A. (2001). Accelerometric Radiation Simulation for the September 26, 1997 Umbria-Marche (Central Italy) Main Shocks. *Annali di Geofisica* **44**, 605–617.
- Emolo, A., Zollo, A. (2005). Kinematic Source Parameters for the 1989 Loma Prieta Earthquake from the Nonlinear Inversion of Accelerograms, *Bull. Seism. Soc. Am.* **95**, 981–994.
- Frankel, A. (1991). High-Frequency Spectral Falloff of Earthquakes, Fractal Dimension of Complex Rupture, b Value, and the Scaling of Strength on Faults, *Journal of Geophysics* **96**, 6291–6302.
- Frankel, A. (1995). Simulating Strong Motions of Large Earthquakes Using Recordings of Small Earthquakes: the Loma Prieta Mainshock as a Test Case. *Bull. Seism. Soc. Am.* **85**, 1144-1160.
- Gallovič, F., Brokešová, J. (2004). On strong ground motion synthesis with k^{-2} slip distributions, *J. Seismology* **8**, 211–224.
- Gallovič, F., Burjánek, J. (2006). Directivity in strong ground motion modeling methods, *submitted to Annali di Geofisica*.
- Guatteri, M., P.M. Mai, and G.C. Beroza (2004). A pseudo-dynamic approximation to dynamic rupture models for strong ground motion prediction, *Bull. Seis. Soc. Am.* **94**, 2051–2063.
- Hanks, T. C. (1982). fmax. *Bull. Seism. Soc. Am.* **72**, 1867–1879.
- Hartzell, S. (1978). Earthquake aftershocks as Green's functions, *Geophys. Res. Lett.* **5**, 1-4.
- Hartzell, S., S. Harmsen, A. Frankel, and S. Larsen (1999), Calculation of broadband time histories of ground motion: comparison of methods and validation using strong-ground motion from the 1994 Northridge earthquake, *Bull. Seism. Soc. Am.* **89**, 1484–1504.
- Hartzell, S., Guatteri, M., Mai, P.M., Liu, P.-Ch., Fisk, M. (2005). Calculation of Broadband Time Histories of Ground Motion, Part II: Kinematic and Dynamic

- Modeling Using Theoretical Greens Functions and Comparison with the 1994 Northridge Earthquake, *Bull. Seism. Soc. Am.* *95*, 614–645.
- Hartzell, S. H., Heaton, T. H. (1986). Rupture History of the 1984 Morgan Hill, California, Earthquake from the Inversion of Strong Motion Records, *Bull. Seism. Soc. Am.* *76*, 649–674.
- Heaton, T. H. (1990). Evidence for and implications of self-healing pulses of slip in earthquake rupture, *Phys. Earth Planet. Interiors* *64*, 1–20.
- Herrero, A., Bernard, P. (1994). A Kinematic Self-Similar Rupture Process for Earthquakes, *Bull. Seism. Soc. Am.* *84*, 1216–1228.
- Horikawa, H. (2001). Earthquake Doublet in Kagoshima, Japan: Rupture of Asperities in a Stress Shadow, *Bull. Seism. Soc. Am.* *91*, 112–127.
- Irikura, K., Kamae, K. (1994). Estimation of Strong Ground Motion in Broad-frequency Band Based on a Seismic Source Scaling Model and Empirical Green's Function Technique, *Annali di Geofisica XXXVII*, 1721–1743.
- Ji, C., Wald, D.J., Helmberger, D.V. (2002). Hector Mine, Source description of the 1999 Hector Mine, California, earthquake, part II: Complexity of slip history, *Bull. Seism. Soc. Am.* *92*, 1208–1226.
- Joyner, W. B. (1991). Directivity for Non-uniform Ruptures. *Bull. Seism. Soc. Am.* *81*, 1391–1395.
- Kostrov, B. V. (1964). Self-similar problems of propagation of shear cracks, *J. App. Math. Mech.* *28*, 1077–1087.
- Mai, P.M., Beroza, G.C. (2003). A hybrid method for calculating near-source, broadband seismograms: application to strong motion prediction, *Phys. Earth Planet. Interiors* *137*, 183–199.
- Novotný, O., Zahradník, J., Tselentis, G. A. (2001). Northwestern Turkey Earthquakes and the Crustal Structure Inferred from Surface Waves Observed in Western Greece, *Bull. Seism. Soc. Am.* *91*, 875–879.
- Pacor, F., Cultrera, G., Mendez, A., Cocco, M. (2005). Finite Fault Modeling of Strong Ground Motions Using Hybrid Deterministic-Stochastic Approach, *Bull. Seism. Soc. Am.* *95*, 225–240.
- Roumelioti, Z., Dreger, A., Kiratzi, Theodoulidis, N. (2003). Slip distribution of the 7 September 1999 Athens earthquake inferred from an empirical Greens function study, *Bull. Seism. Soc. Am.* *93*, 775–782.
- Roumelioti, Z., Kiratzi, A., Theodoulidis, N. (2004). Stochastic Strong Ground-Motion Simulation of the 7 September 1999 Athens (Greece) Earthquake, *Bull. Seism. Soc. Am.* *94*, 1036–1052.
- Si, H., Midorikawa, S. (1999). New attenuation relationships for peak ground acceleration and velocity considering effects of fault type and site condition, *J. Struct. Constr. Eng., AIJ*, *523*, 63–70.

- Skarlatoudis, A. A., C. B. Papazachos, B. N. Margaritis, N. Theodulidis, Ch. Papaioannou, I. Kalogeras, E. M. Scordilis, and V. Karakostas (2003), Empirical peak ground-motion predictive relations for shallow earthquakes in Greece, *Bull. Seism. Soc. Am.* *93*, 2591-2603.
- Spudich, P., Archuleta, R. J. (1987). Techniques for Earthquake Ground-Motion Calculation with Applications to Source Parametrization of Finite Faults, in *Seismic Strong Motion Synthetics*, B. A. Bolt (Editor), Academic Press, Orlando, Florida, 205–265.
- Tselentis, G. A., and J. Zahradník (2000), The Athens Earthquake of 7 September 1999, *Bull. Seism. Soc. Am.* *90*, 1143–1160.
- Wald, D. J., Heaton, T. H. (1994). Spatial and Temporal Distribution of Slip for the 1992 Landers, California, Earthquake, *Bull. Seism. Soc. Am.* *84*, 668–691.
- Wald, D. J., Heaton, T. H., Hudnut, K. W. (1996). The slip history of the 1994 Northridge, California, earthquake determined from strong motion, teleseismic, GPS and leveling data, *Bull. Seism. Soc. Am.* *86*, S49–S70.
- Wells, D.L., Coppersmith, K.J. (1994). New empirical relationship among magnitude, rupture length, rupture width, rupture area, and surface displacement, *Bull. Seism. Soc. Am.* *84*, 974–1002.
- Zeng, Y., Anderson, J. G., Yu, G. (1994). A composite source model for computing realistic synthetic strong ground motions, *Geophys. Res. Lett.* *21*, 725–728.
- Zollo, A., Bobbio, A., Emolo, A., Herrero, A., De Natale, G. (1997). Modeling of Ground Acceleration in the Near Source Range: the Case of 1976, Friuli Earthquake (M=6.5), Northern Italy. *J. Seismology* *1*, 305–319.

Figure captions

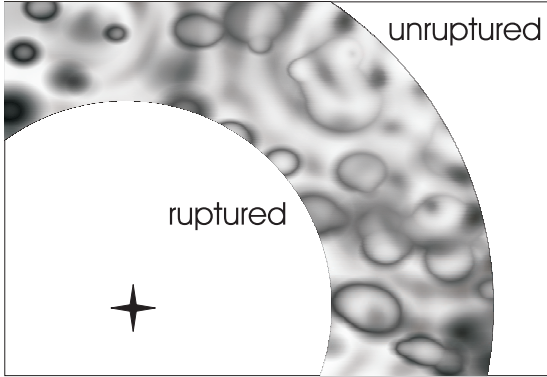


Figure 1: An illustrative picture of the hybrid source model. It corresponds to a snapshot of the slip velocity (the more dark the color, the larger the slip velocity). The star indicates a nucleation point. Note that the small-scale chaotic rupturing takes place within the deterministic large-scale slip pulse.

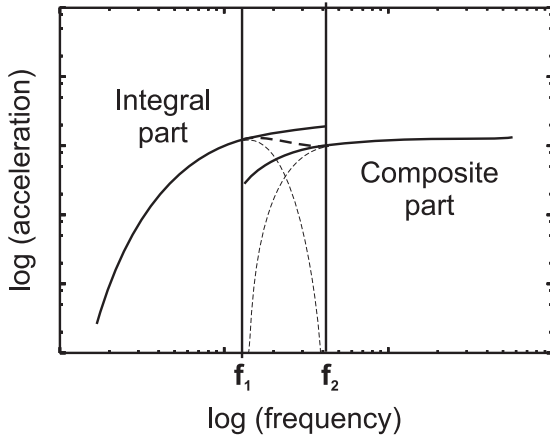
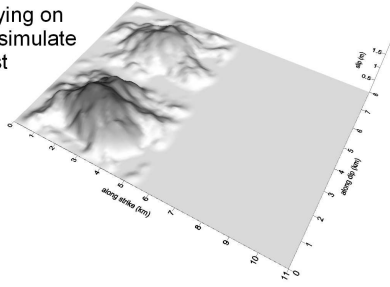
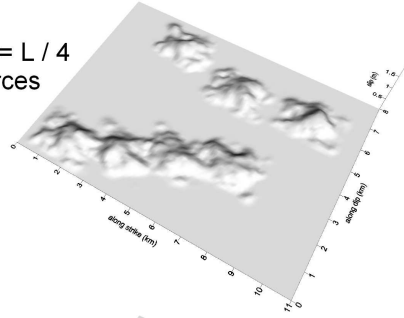


Figure 2: A sketch of the hybrid combination of the integral and composite synthetics (bold solid lines) in the frequency domain. In the cross-over frequency zone (between bounding frequencies f_1 and f_2) the synthetics are multiplied by weighting functions $\sin^2(x)$ and $\cos^2(x)$, with $x = \frac{\pi}{2} \frac{f-f_1}{f_2-f_1}$ (thin dashed lines) and summed up (bold dashed line). This operation is performed for both the real and imaginary parts of the spectrum. Note that the possible step in spectral levels in the cross-over zone depends mainly on the mutual amount of directivity in the integral and composite models. Moreover, the transition could be smoother due to propagation effects and/or may be masked by the oscillatory character of the Fourier spectra.

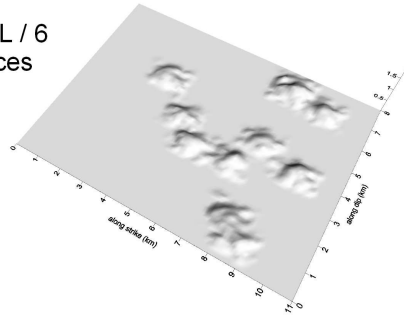
Level 2, $l = L / 2$
 3 subsources
 (two of them lying on each other to simulate a high-contrast asperity)



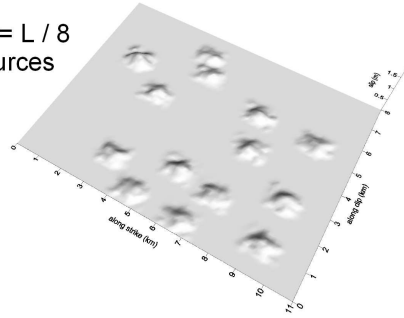
Level 4, $l = L / 4$
 7 subsources



Level 6, $l = L / 6$
 11 subsources



Level 8, $l = L / 8$
 15 subsources



Total slip
 63 subsources
 (levels 2 - 8)

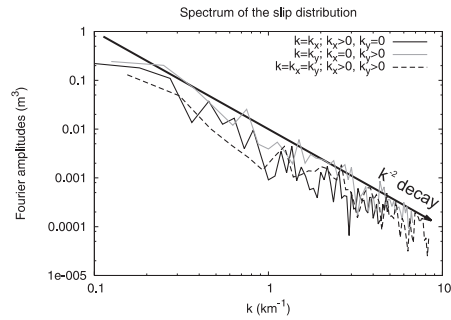
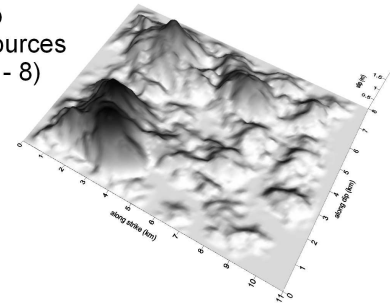


Figure 3: Slip distribution constructed from the subsource database. Top panels show examples of 4 selected levels. The resulting slip distribution (sum of all seven levels 2 – 8) is shown at the bottom left. Three cross-sections of its spatial amplitude Fourier spectrum are shown at the bottom right. The bold solid line indicates the k -squared decay. Note that level $n = 1$ is neglected. It would correspond to a slip patch over the whole fault, which is, however, not observed in slip inversions of medium-to-large sized earthquakes.

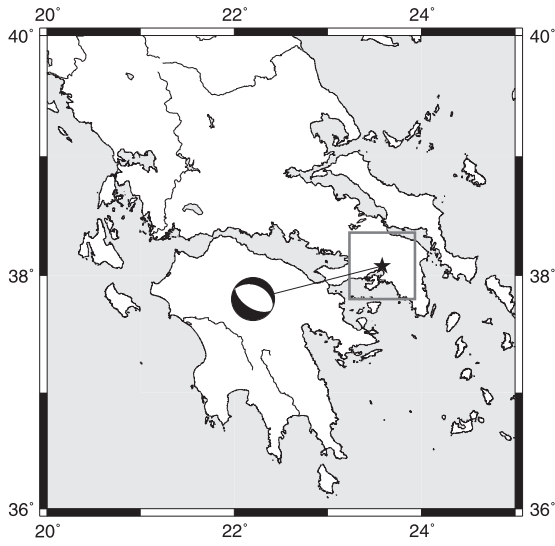


Figure 4: Map of Greece with the 1999 Athens earthquake epicenter (star) and its focal mechanism (*Tselentis and Zahradník, 2000*). The area of interest is depicted as a gray rectangle.

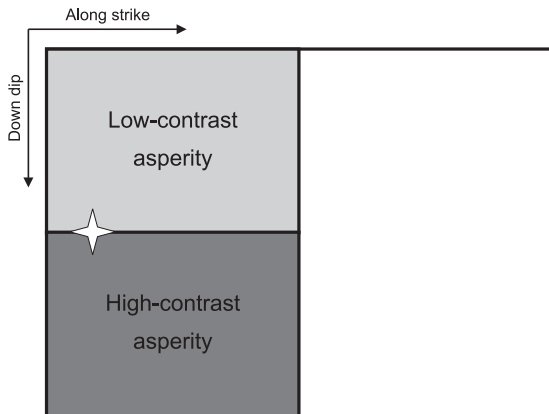


Figure 5: Scheme of asperities and nucleation point (star) location for the Athens earthquake model. An example of one realization of the corresponding slip distribution can be seen in Fig. 3.

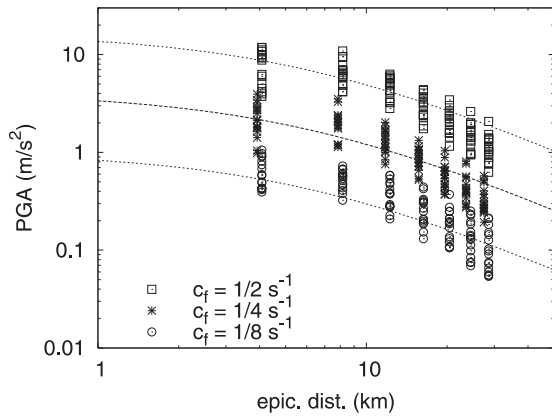


Figure 6: PGAs (symbols) obtained at receivers shown at the top of Fig. 7 for three different values of c_f , drawn as a function of epicentral distance. To distinguish the three choices of c_f better, all the symbols are slightly shifted to the right or left of the correct horizontal position. Empirical attenuation curve (bold dashed line) for $M_w = 5.9$ (Skarlatoudis et al., 2003) and its $\pm 2\sigma$ uncertainty (thin dashed lines) are shown.

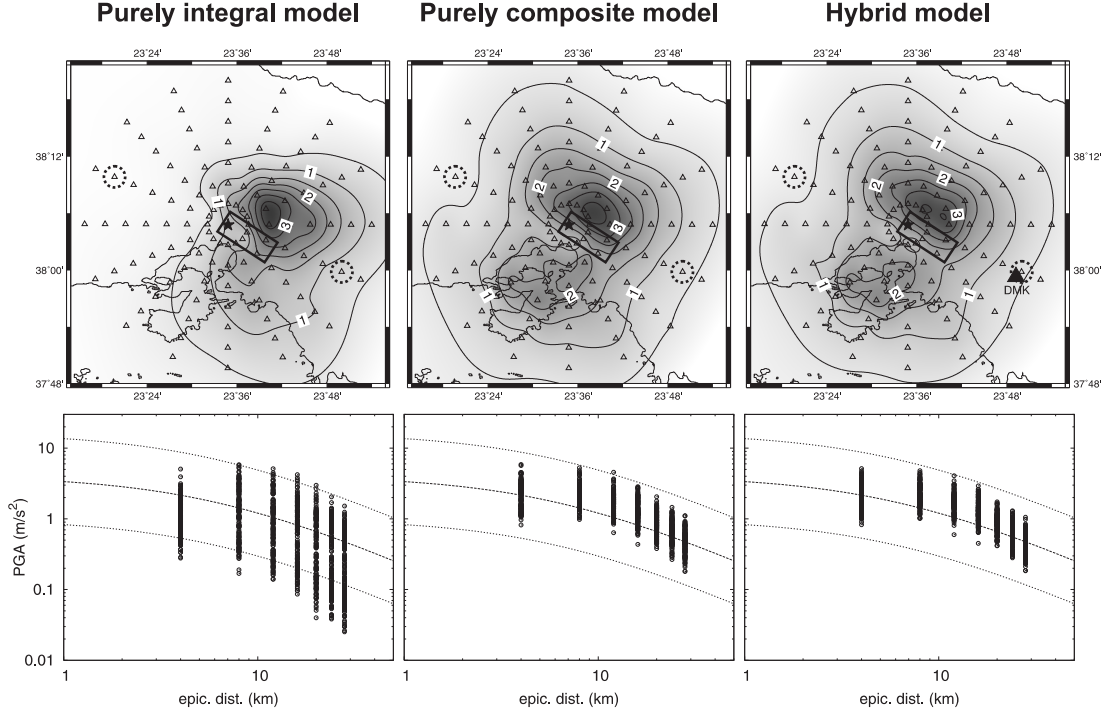


Figure 7: Comparison of synthetic horizontal PGAs (in m/s^2) provided by the purely integral k -squared method with k -dependent rise time (left), the purely composite method (middle) and their hybrid combination (right). Top: log-normal mean PGAs obtained from 10 random slip realizations, i.e. location of subsources (preserving the locations of asperities). The epicenter (star), virtual receivers (triangles) and surface projection of the fault (dark rectangle) are shown. The area corresponds to the one shown as the gray rectangle in Fig. 4. Circles denote stations used in Fig 8. The black triangle marks the location of station DMK (see Fig. 9). Bottom: PGAs (points) obtained at receivers shown at the top of this figure, drawn as a function of epicentral distance. Results for all the 10 realizations are included. The bold dashed line is the empirical attenuation curve for $M_w = 5.9$ (Skarlatoudis *et al.*, 2003). The thin dashed lines represent its $\pm 2\sigma$ uncertainty (σ being the standard deviation).

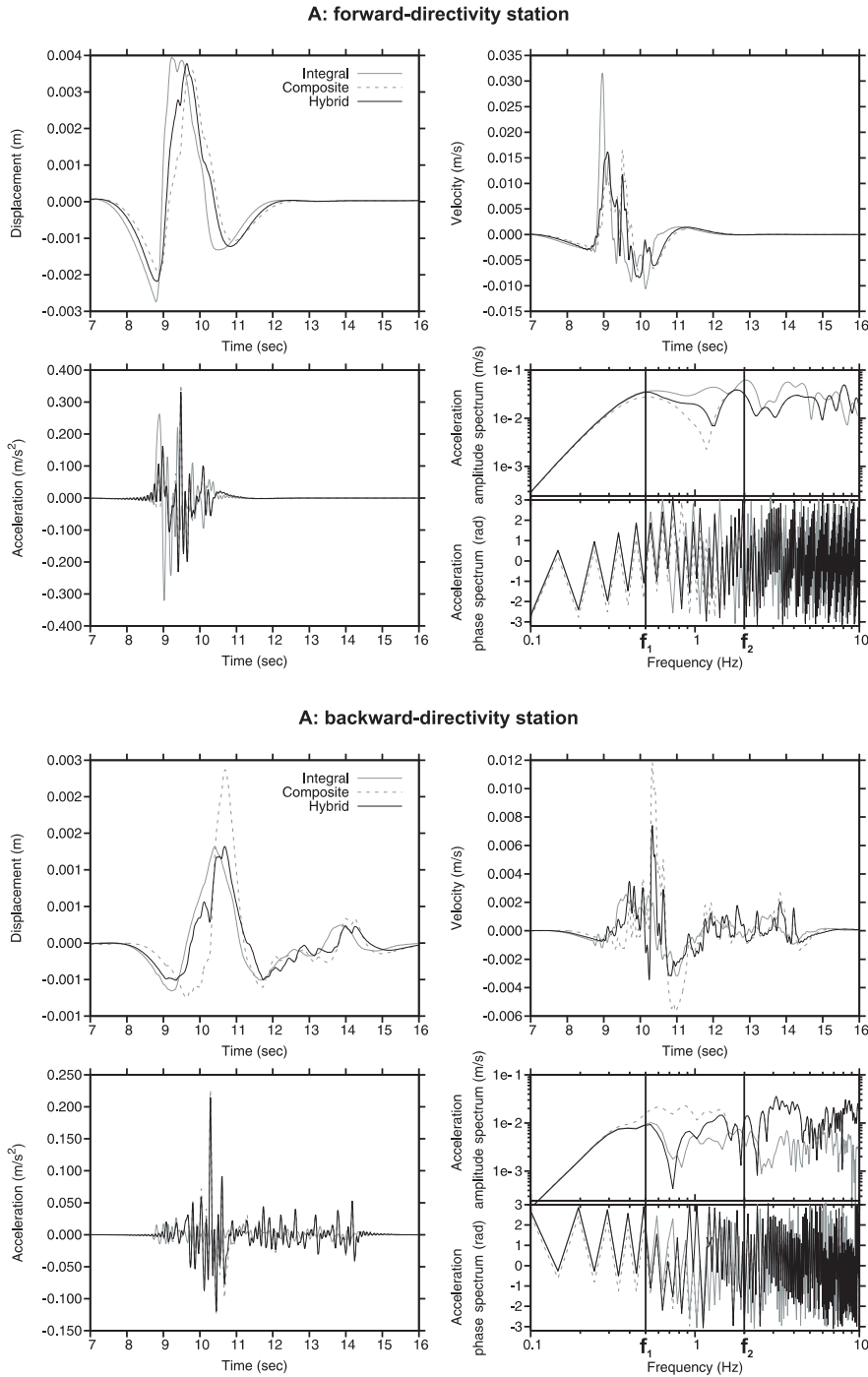


Figure 8: Examples of synthetic seismograms (displacement, velocity and acceleration) for 2 stations situated 24 km from the epicenter in the forward (A) and backward (B) directions with respect to rupture propagation (see Fig. 7 for their positions), obtained by the use of purely integral and purely composite models, and by their hybrid combination (see legend). Note that the amplitude scales are different for backward- and forward-direction stations. The bottom right two plots in A and B are the corresponding acceleration Fourier amplitude and phase spectra. Frequencies f_1 and f_2 mark the cross-over region.

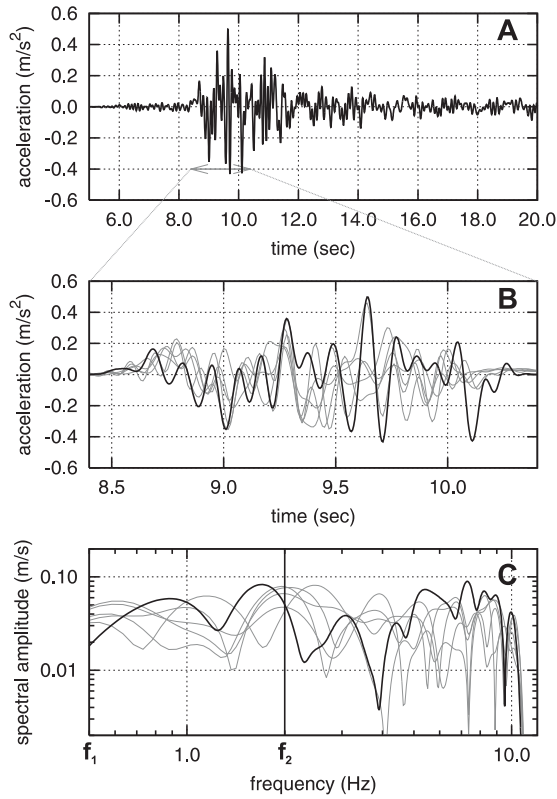


Figure 9: Comparison of the transverse component of the observed and synthetic accelerations calculated by the hybrid approach at station DMK (see Fig. 7). A: Full trace of the recording, the gray double headed arrow indicates 2 sec part (8.4-10.4 sec) considered as the direct S-wave. B: Expanded 2 sec part of the observed record (black curve) and the synthetics for 5 realizations of the subsurface distribution (gray curves). C: Comparison of Fourier spectra of the waveforms shown in B. The cross-over range is indicated by f_1 and f_2 .

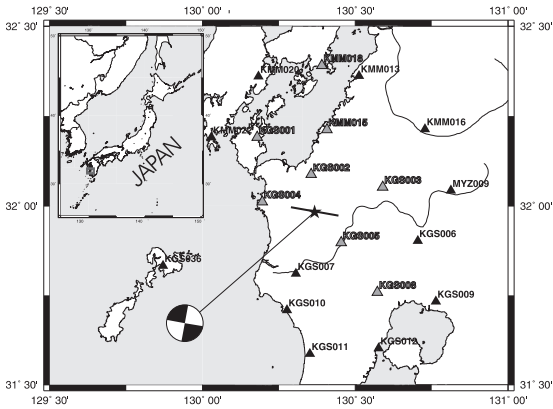


Figure 10: Configuration of source and stations for the Kagoshima earthquake in the area of interest (indicated by the gray rectangle in the inset map of Japan). The epicenter location is shown as the star and the focal mechanism of the earthquake is indicated (Horikawa, 2001). The black line depicts the fault surface projection. Stations are represented by the triangles. The selected subset of receivers subjected to comparison between observed data and synthetics is marked in gray.

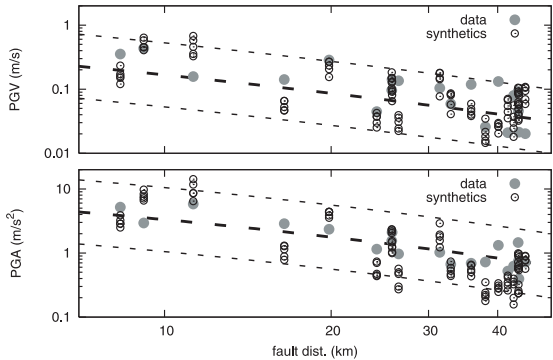


Figure 11: Comparison of simulated PGAs (left) and PGVs (right) with the observed plotted with respect to the fault distance. For each station the PGAs and PGVs, obtained for 5 realizations of the random subsources position on the fault, are shown. The bold line corresponds to the empirical attenuation curve for Japan ($M_w = 6.1$) by Si and Midorikawa (1999). The thin lines represent its $\pm 2\sigma$ uncertainty.

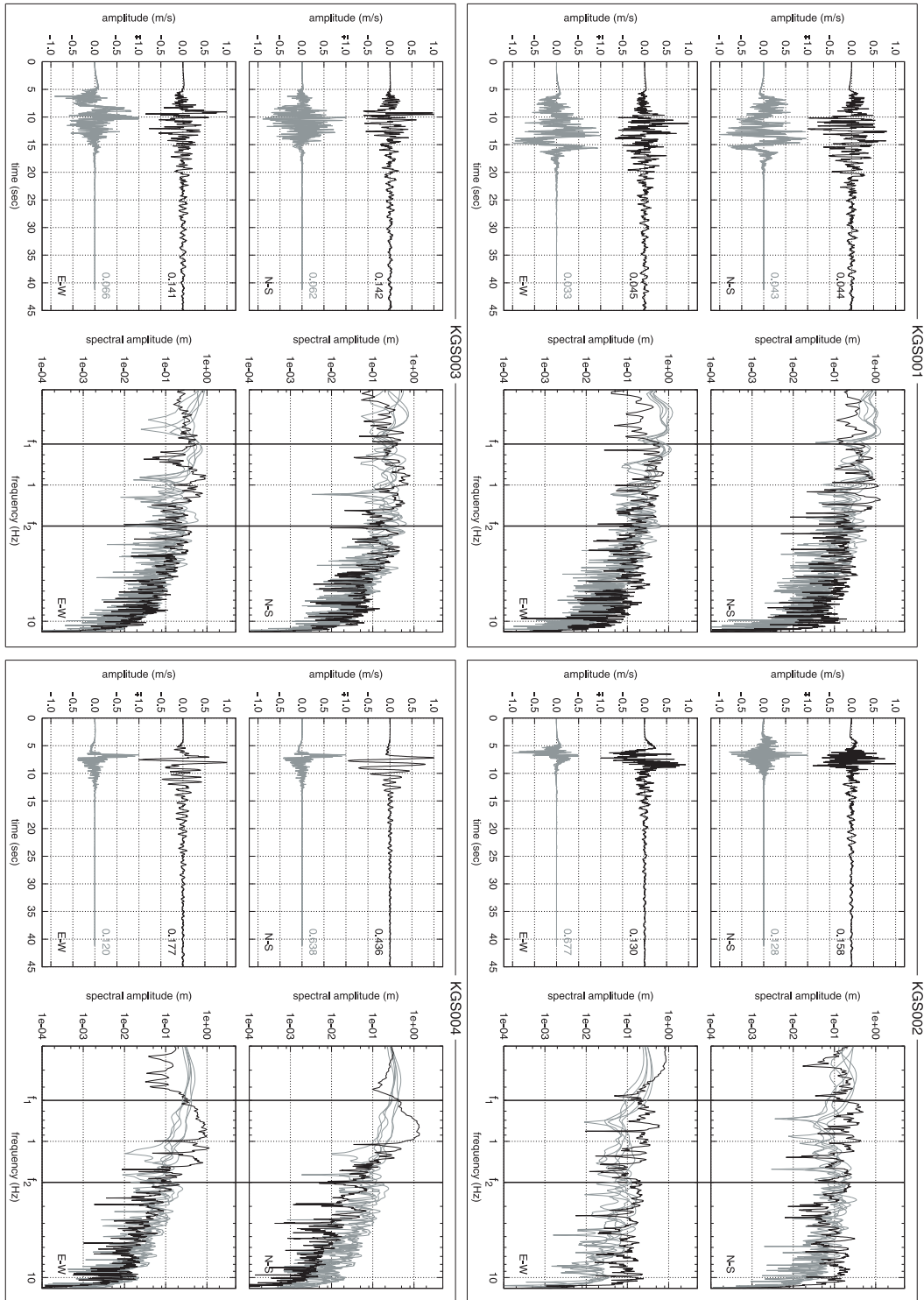


Figure 12: Observed horizontal components of velocities plotted with 5 corresponding synthetics obtained by the use of different realizations of the subsource distribution (keeping asperity unchanged). Each panel corresponds to a given selected station (depicted as gray triangles in Fig. 10). The top and bottom traces (left in each panel) are the observed and simulated velocigrams, respectively. The waveforms are normalized and their peak values are displayed close to the seismogram trace. The comparison of observed (black) and synthetic (gray) velocity amplitude spectra (not normalized) are shown on the right of each panel. Frequencies f_1 and f_2 denote the cross-over zone.

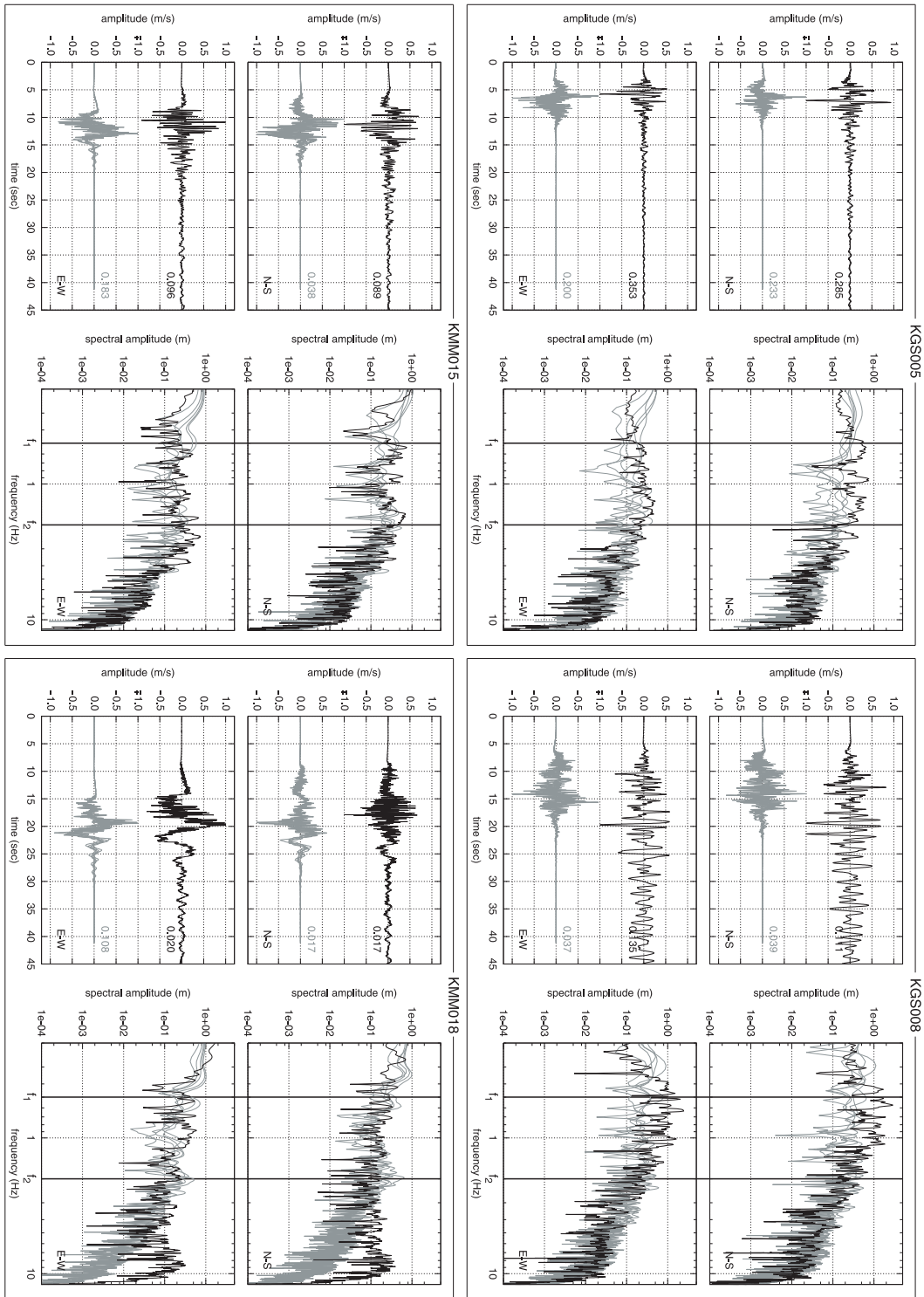


Figure 12: cont.

Tables

Parameter	Athens earthquake (<i>Tselentis and Zahradník, 2000</i>)	Kagoshima earthquake (<i>Horikawa, 2001</i>)
Lat. (N)	38.08°	31.98
Long. (E)	23.58°	130.37
Hypocentral depth [km]	12.0	7.6
Fault-top depth [km]	8.8	1.1
Moment [Nm]	$7.8 \cdot 10^{17}$	$1.5 \cdot 10^{18}$
Strike	123°	280°
Dip	55°	90°
Rake	-84°	0°
v_r [km/s]	2.8	2.5
L [km]	11	15
W [km]	8	10
τ_{max} [sec]	1.0	1.0
L_0 [km]	2.8	2.5

Table 1: Model parameters of earthquakes under study.

thickness (km)	$v_p(km/s)$	$v_s(km/s)$	$\rho(g/cm^3)$
1	2.67	1.50	2.50
1	4.45	2.50	2.50
3	5.70	3.20	2.84
13	6.00	3.37	2.90
21	6.40	3.60	2.98
∞	7.90	4.44	3.28

Table 2: Parameters of crustal model used in the Athens earthquake modeling (so-called MA, see *Tselentis and Zahradník, 2000*,).

thickness (km)	v_p (km/s)	v_s (km/s)	ρ (g/cm ³)	Q_P	Q_S
0.5	2.8	1.62	2.1	80	40
4.5	4.9	2.83	2.3	300	150
10.0	6.0	3.46	2.7	300	150
20.0	6.7	3.87	3.1	500	250
∞	7.8	4.50	3.4	1000	500

Table 3: Velocity structure used in the Kagoshima earthquake modeling (from *Horikawa, 2001*).